frontiers | Frontiers in Earth Science

TYPE Original Research
PUBLISHED 13 January 2023
DOI 10.3389/feart.2022.1042539

OPEN ACCESS

EDITED BY
Jun Zhao,
Anhui University of Science and Technology, China

REVIEWED BY
Qi Yao,
China Earthquake Administration, China
Feng Du,
China University of Mining and Technology, China
Zou Quanle,
Chongqing University, China
Zhengzheng Cao,
Henan Polytechnic University, China
Ke Yang,
Anhui University of Science and Technology, China

*CORRESPONDENCE
Jinrong Cao,
jin-rongcao@cumt.edu.cn
Linming Dou,
lmdou@126.com

SPECIALTY SECTION
This article was submitted to Geohazards and Georisks, a section of the journal Frontiers in Earth Science

RECEIVED 12 September 2022
ACCEPTED 31 October 2022
PUBLISHED 13 January 2023

CITATION
Cao J, Dou L, He J, Zhu G, Wang Z, Bai J and Han Z (2023), Failure mechanism and control of coal bursts triggered by mining induced seismicity in steeply inclined and extra thick coal seam. *Front. Earth Sci.* 10:1042539. doi: 10.3389/feart.2022.1042539

Failure mechanism and control of coal bursts triggered by mining induced seismicity in steeply inclined and extra thick coal seam

Jinrong Cao[1]*, Linming Dou[1,2]*, Jiang He[1], Guangan Zhu[3], Zhengyi Wang[4], Jinzheng Bai[1] and Zepeng Han[1]

[1]School of Mines, China University of Mining and Technology, Xuzhou, China, [2]Jiangsu Engineering Laboratory of Mine Earthquake Monitoring and Prevention, Xuzhou, China, [3]School of Energy Engineering, Xi'an University of Science and Technology, Xi'an, China, [4]School of Civil Engineering and Architecture, Changzhou Institute of Technology, Changzhou, China

With the increase in mining depth, coal bursts have become a major challenge in the safe mining of steeply inclined and extra thick coal seams (SIETCSs). Based on a typical mining induced seismicity triggered coal burst (MSTCB) in SIETCS, a large-scale numerical model was developed using the Universal Distinct Element Code. The numerical model was calibrated and validated by laboratory results and field observations. The stress evolution, crack development and ejection velocity patterns in the MSTCB were analysed, and the effect of mining induced seismicity vibration velocity on the MSTCB was discussed. The results show that a triangular static stress concentration zone is formed in the coal on the roof side. And the high-energy mining induced seismicity leads to high dynamic stresses in the coal at the roof side rib and top of the headentry. Coal bursts occur under the superposition of static and dynamic stresses. The MSTCB results in tensile failure near the headentry surface and shear failure in the depth. The vibration velocity has a significant effect on the roof side rib and top of the headentry, while it has only a slight effect on the working face rib and bottom of the headentry. The dynamic stress and ejection velocity in the roof side rib and top of the headentry are positively correlated with the vibration velocity. Finally, measures for MSTCB prevention were proposed. The findings presented in this study can provide guidance for the prevention and control of MSTCBs in SIETCSs.

KEYWORDS

steeply inclined and extra thick coal seam, coal burst, mining induced seismicity, UDEC, crack development

1 Introduction

As a violent dynamic failure in underground coal mining, coal bursts occurred worldwide with the increasing mining depth (Jiang et al., 2017; Ptáček, 2017; Mark, 2018), causing many casualties (Zhang et al., 2017) and other disasters (Du et al., 2020; Wang and Du, 2020). Coal bursts can be classified into self-initiated and remotely mining-induced seismicity triggered based on its mechanisms (Dou and He, 2001; Mottahedi and Ataei, 2019). Seismic events occur frequently in large-scale mining due to roof breakage, fault slip, coal pillar failure, etc. (Dou and He, 2001; Stec, 2007). Compared to self-initiated coalburst, mining-induced seismicity triggered coal bursts (MSTCBs) are more likely to occur in coal mines (Dou and He, 2001). In recent years, MSTCBs have been reported during horizontal section mining of steeply inclined and extra thick coal seams (SIETCSs) in China (Wang et al., 2019b; He et al., 2020). It is significant to investigate the mechanism and control of MSTCBs in SIETCSs.

To reveal the mechanism of MSTCBs, (Dou et al., 2015) proposed the coupled theory of static and dynamic stresses from the perspective of stress changes during coal bursts. He et al. (2017) analyzed the stress distribution during rockburst triggered by mine tremors and proposed a method to evaluate rockburst risk in mining. According to Cai et al. (2021), the dynamic stress from fault activation is a key factor in the coal burst triggered by fault. Dai et al. (2021) investigated the MSTCB theoretically and developed a critical index system to descript the remotely triggered coal bursts quantitatively. And many prevention measures had been applied in the field to control MSTCBs, such as optimization of mining design (Dou and He, 2001; Jiang et al., 2017), destress blasting in the roof (Konicek et al., 2011; Konicek et al., 2013), as well as hydraulic fracturing of hard and thick rock (Shapiro et al., 2006; He et al., 2012a). However, current studies mainly focus on horizontal and gently inclined coal seams. Due to the special geological conditions and mining methods, MSTCBs caused by horizontal section mining of SIETCSs are significantly different from those of horizontal and gently inclined coal seams. (Wang et al., 2019c). reported an MSTCB occurred on the working face in SIETCS and mechanically investigated its mechanism, results showed that abutment pressure near the roof was the main source of static stress. Xie et al. (2019) observed the roof deformation caused by mining two adjacent working faces in SIETCS based on physical simulation and found that mining of the lower working face led to a secondary movement of the roof. Yang et al. (2020b). analyzed the temporal-spatial evolution characteristics of dynamic failure in SIETCS and identified the stress concentration areas around the roadway. Wang et al. (2022) studied the stress redistribution caused by horizontal section mining in SIETCS, and found that there is high shear stress in the bottom coal under the effect of "shear-clamping". Dynamic stress plays a critical role in MSTCBs (He et al., 2012; Dou et al., 2014). Yun et al. (2017) performed field monitoring of support pressure in the working face and observed that the dynamic load coefficients caused by roof breakage varied between 1.45 and 1.52 during mining of the SIETCS. He et al. (2020) investigated the rock burst mechanism of two adjacent working faces in SIETCS, and the results indicated that fractures of the roof and rock pillar were the main dynamic stress sources of rock bursts. Yang et al. (2019) concluded that topping-slumping failure would occur after mining in SIETCS, resulting in strong dynamic loads. Lai et al. (2021) found that the roof structure in SIETCS would experience periodic "balance-instability" during mining, which is accompanied by energy accumulation and release. Cao et al. (2020) used numerical simulation to study the development of roof structure and the evolution of stress during mining in SIETCS, and concluded the sources of static and dynamic stress. Cui et al. (2019) proposed a surface filling technology to reduce the risk of dynamic hazards caused by mining of SIETCS. In addition, there are also some studies on precursory warnings for coal bursts in SIETCSs based on field monitoring (He et al., 2019; Wang et al., 2020; Li et al., 2021b).

The above-mentioned studies have enriched our understanding of MSTCBs in SIETCSs. At present, many meaningful results have been derived, such as the asymmetric distribution of mining-induced stresses, the periodicity breakage of the steeply inclined roof, as well as the identification of static and dynamic stress sources, etc. However, more details of the dynamic failure process of MSTCBs in SIETCSs need to be further investigated, including stress evolution, the development of cracks, ejection velocity patterns, and the effect of the mining induced seismicity strength on MSTCBs. Studies in these aspects also are important for the prevention and control of MSTCBs in SIETCSs.

Taking an MSTCB that occurred in a typical SIETCS as the engineering background, this paper investigates the mechanism and control of MSTCBs in SIETCSs by using the Universal Distinct Element Code (UDEC) software (Itasca 2014). First, the engineering background and damage characteristics of the MSTCB were present. Second, a large-scale numerical model to reproduce the complete process of the MSTCB was developed. Third, the stress evolution, crack development and ejection velocity during the MSTCB were analysed, and the effect of the vibration velocity of mining induced seismicity on the MSTCB was studied. Finally, the mechanism and prevention measures of the MSTCB in SIETCS were proposed. Field monitoring indicates that the measures significantly decrease the risk of MSTCB in SIETCS.

2 Engineering background and damage characteristics

2.1 Engineering overview

The thickness of the SIETCS in Yaojie No.3 Coal Mine is in the range of 36–115 m, with an inclination angle of about 60°.

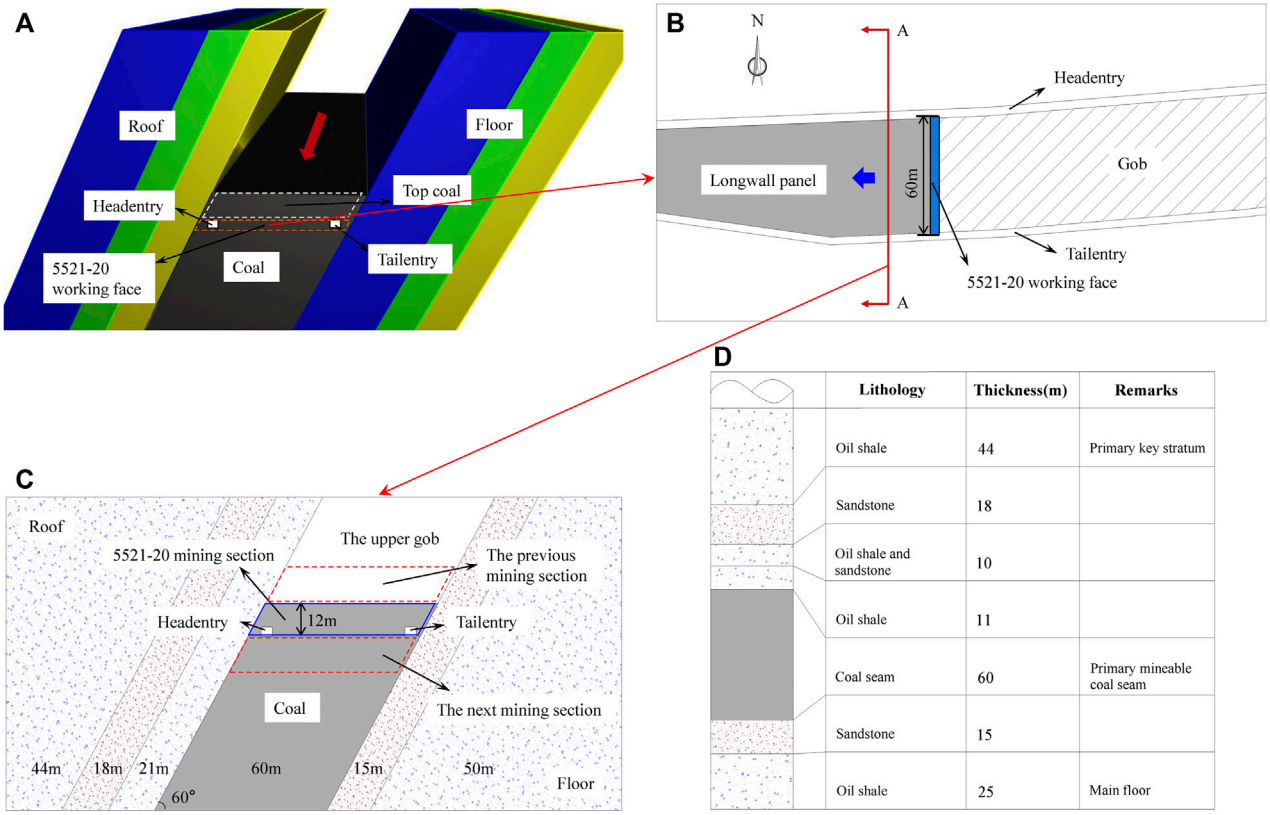

FIGURE 1
The coal mine: **(A)** the horizontal section full-mechanized top-coal caving mining in SIETCS, **(B)** mining layout, **(C)** cross-section of mining area perpendicular to mining advance, and **(D)** geological profile.

According to the classification standard of coal seams in China, coal seams with a thickness greater than 8 m are classified as extra thick coal seams. Coal seams with an inclination angle greater than 45° are classified as steeply inclined coal seams. Thus, the coal seam in Yaojie No.3 Coal Mine is a typical SIETCS. The horizontal section full-mechanized top-coal caving mining technology is adopted, and a longwall working face is arranged in each horizontal section. As shown in Figure 1A, the 5,521-20 working face is located in a section with a height of 12 m, and the mining to caving height ratio is 1:3. The design of the 5,521-20 working face is shown in Figures 1B,C, the width of the 5,521-20 working face is variable due to the change in coal seam thickness, the maximum width is about 60 m. The 5,521–20 headentry and the 5,521-20 tailentry are set in the coal seam near the roof and floor respectively and there is a coal pillar with a width of 6 m between the headentry and the roof. The mining depth of the 5,521-20 working face is 470–530 m. *In-situ* stress measurements were carried out, and the results showed that the initial horizontal and vertical stresses were 22 MPa and 13 MPa, respectively. The geological profile is shown in Figure 1D, there are thick sandstone and oil shale in the roof, and a 44 m thick oil shale is the main key layer according to the key layer theory (Qian et al., 2000). With the increase of mining depth, the upper gob became larger, and the number of mine tremors caused by the roof breakage increased, which eventually caused a serious coal burst in the headentry.

2.2 Coal burst in the headentry

On June 29, 2016, accompanied by a high-energy seismic event in the roof, an MSTCB occurred in the headentry of the 5,521-20 working face. Figure 2 shows the location of the MSTCB and some *in situ* recorded photos. As shown in Figure 2A, a total of 44 m of the headentry in front of the working face was damaged, including a 10 m area near the working face that was severely damaged. Under the effect of the seismic event on the roof, some equipment overturned, and some artificial support units failed, as shown in Figure 2B, and it is worth noting that both the rollover of equipment and the sliding of support units have the same direction from the roof side to the working face side. As illustrated in Figure 2C, the MSTCB resulted in large

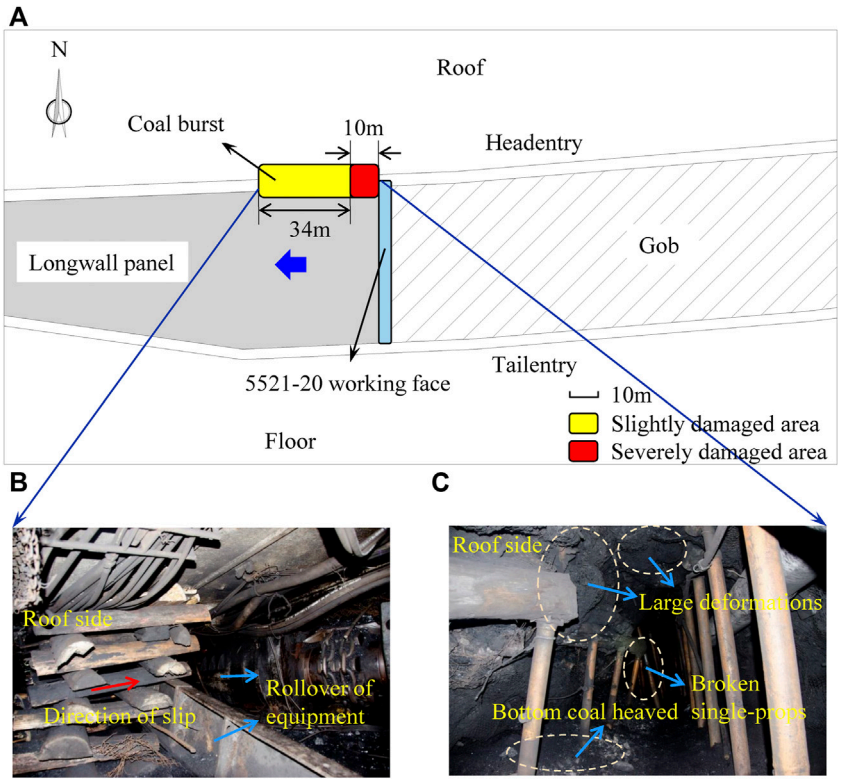

FIGURE 2
The MSTCB in the 5,521–20 headentry: **(A)** location of coal burst, **(B)** rollover of equipment, and **(C)** typical failures in the headentry.

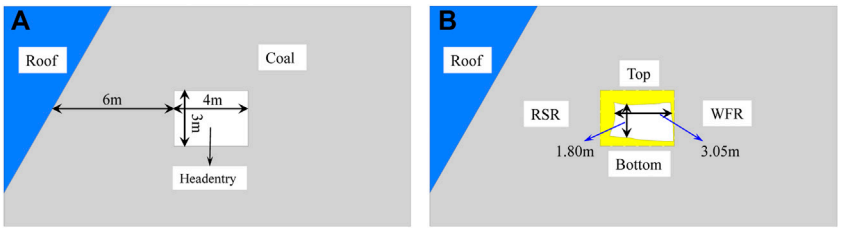

FIGURE 3
Cross-section of the headentry: **(A)** before the MSTCB, and **(B)** after the MSTCB.

deformation on the roof side and top of the headentry, and the cables and wire mesh were damaged by the fractured coal, and it can be seen that the deformation of the roof side wall was mainly concentrated on the upper part. The bottom coal was heaved. In addition, a large number of single-props failed. After the MSTCB occurred, field measurements were carried out on the headentry. A sketch (see Figure 3) of the headentry before and after the MSTCB illustrates the damage and deformation pattern. Before the MSTCB, the width and height of the headentry were 4 m and 3 m respectively, as shown in Figure 3A. The sketch of the headentry after the MSTCB is shown in Figure 3B, we divided the coal around the headentry into four zones, they are the top, bottom, roof side range (RSR), and working face range (WFR). According to the field measurement results, the maximum deformation of the top, bottom, RSR, and WFR were 0.7, 0.5, 0.8, and 0.15 m respectively, and the convergence of the roof to the bottom and the RSR to the WFR reached 1.2 and 0.95 m respectively. It is also notable that the maximum deformation of the bottom is located on the roof side. It can be concluded that the damage to the headentry caused by the MSTCB has

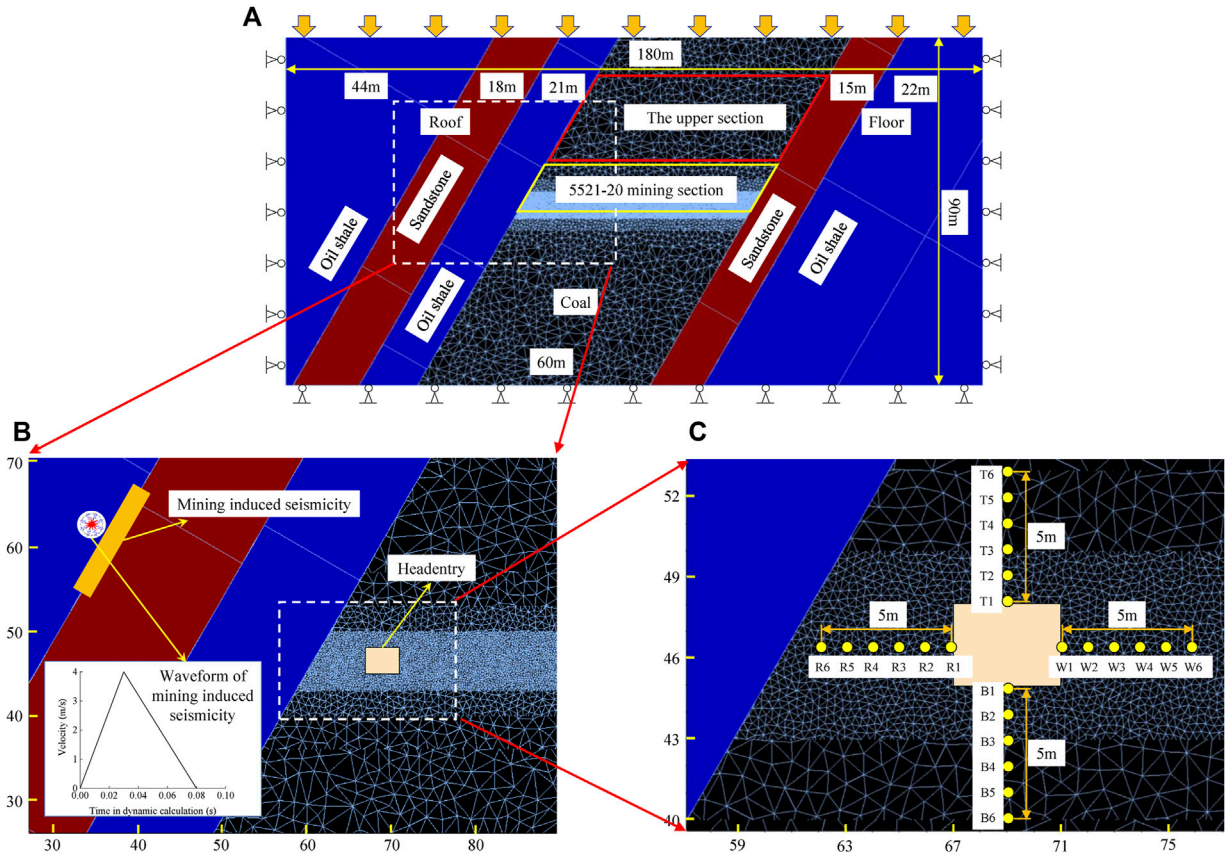

FIGURE 4
UDEC numerical model: **(A)** overview of the model, **(B)** detail incl. hypocentre of mining induced seismicity, and **(C)** detail of 5,521–20 headentry area (T, R, B, and W indicate the locations of monitoring).

significant asymmetric characteristics, and the main large deformation areas are the RSR, top, and bottom of the headentry. Compared with the area on the WFR, more severe dynamic damage occurred in the area near the roof. When the MSTCB occurred, the pressures of the hydraulics arranged near the roof were observed to increase significantly. The pressures of 25# and 30# hydraulic were up to 46 and 44 MPa, respectively. In comparison with the previous day, the pressures increased by 360% and 340%, respectively, indicating that strong dynamic stress was developed in the coal on the roof side.

3 Numerical simulation

3.1 Modelling method

UDEC, a two-dimensional numerical program, simulates the quasi-static or dynamic response to the loading of a discontinuous medium. The simulated coal and rock consist of a number of deformable blocks and contacts between the blocks. The failures of the contacts are controlled by the stresses acting at the contact and the failure criterion (Itasca 2014). There are two main failure modes for the contacts: shear cracking and tensile cracking. The penetration of contact cracks leads to the formation of macroscopic failure. In this study, the blocks were divided into triangles according to the UDEC-Trigon method (Gao and Stead, 2014). It was shown that the UDEC-Trigon model can successfully reproduce the failure processes including conventional brittle damages or nonlinear dynamic failures caused by mining at the field scale (Gao et al., 2014; Gao and Yang, 2021).

3.2 Model configuration and modelling procedure

Based on the geological data of the 5,521-20 working face, a large-scale numerical model was developed using UDEC. The width of the numerical model is 160 m and the height is 80 m, which consists of the roof, coal and floor, as shown in Figure 4A. The

inclination angle and thickness of the coal seam were set to 60° and 60 m respectively. In the UDEC simulation, if a larger size of the block is chosen, it will be possible to get the wrong failure pattern and mechanism. However, a small block size will be a high computational requirement and time-consuming. To solve this problem, different block sizes were used in different areas in this study, and the small block sizes were used in the areas that need attention. Triangular blocks were used in the coal seam, while rectangular blocks were used in the roof and floor. The average size of the smallest block around the headentry was 0.3 m, which was similar to the size used in the simulation at the field scale (Gao and Stead, 2014), and the size of the blocks in the outer area gradually increased. The gravitational acceleration was set to 9.8 m/(s^2). The static and dynamic calculation modes were employed in order to simulate mining and the MSTCB, respectively. The boundary conditions in the two calculation modes are different. In the static calculation, initial horizontal stress of 22 MPa and initial vertical stress of 13 MPa was applied to the numerical model according to the *in-situ* stress measurements. The boundaries on both sides as well as the bottom were fixed. Vertical stress of 12 MPa was applied to the upper boundary considering the gravity of the overlying rock layers. In the dynamic calculation, the boundary conditions were changed to viscous boundaries to avoid incorrect results caused by the wave reflection on outer boundaries. The stress increase in the surrounding rock caused by the mine tremor is due to the propagation of seismic waves. In addition, the velocity and duration of the seismic waves can be obtained by a microseismic monitoring system in the field. Therefore, a triangular vibration wave is used in this study, and it should be noted that the structural changes caused by the mine tremor are not considered. As shown in Figure 4B, a triangular vibration wave was applied to the roof to simulate the disturbance caused by roof breakage with a peak velocity of 4 m/s and duration of 0.08 s. In this study, Rayleigh damping was adopted. A small value of the damping ratio (e.g., 0.5%) is recommended when large deformation may occur (Itasca 2014). As we know, coal bursts result in large displacement and ejection of coal. Therefore, Rayleigh damping of 0.5 % is employed. In order to quantitatively investigate the stress, velocity, and displacement changes around the headentry during the MSTCB, a large number of monitoring points were set up, as shown in Figure 4C. There are six monitoring points in the top, bottom, RSR, and WFR of the headentry, respectively, and the distance between adjacent monitoring points is 1 m.

A combination of static and dynamic calculation modes was adopted to reproduce the MISTCB in SIETCS. The simulation was divided into two stages. The first stage was carried out in the static calculation mode, in which the upper section located above the 5,521–20 mining section was first excavated after the model was calculated to equilibrium under the given initial conditions, and then, the headentry was excavated. This part focuses on studying the redistribution of stresses and micro-cracking caused by mining. In the second stage, the calculation mode was changed to dynamic, and the vibration wave was applied to the roof. In this section, the MSTCB process is investigated to identify its failure characteristics and mechanisms, including stress evolution, crack development, and velocity patterns.

3.3 Model calibration

The micro-properties of simulated rocks and coal were calculated theoretically and calibrated by laboratory results. First, we obtained the mechanical properties of the rocks and coal in the laboratory, which were referred to as the intact rock properties. Then, considering the difference between the properties of the rock mass and the intact rock, the mechanical properties of the rock mass were estimated theoretically and were the target value for calibration. In this study, the elastic modulus of the rock mass was calculated by the RQD method (Zhang and Einstein, 2004), as shown in Eq. 1, and the uniaxial compressive strength of the rock mass was calculated by the empirical formula proposed by Singh and Seshagiri Rao (2005), and the tensile strength of the rock mass was estimated as 1/10 of the uniaxial compressive strength, as shown in Eq. 2. The properties are shown in Table 1. After obtaining the mechanical properties of the rock mass, two critical micro-properties of the rock mass, normal stiffness and shear stiffness, were calculated by Eqs. 3, 4 (Itasca 2014). Finally, the micro-properties obtained from the above theoretical calculations were calibrated by performing a series of simulated uniaxial compressive tests (UCS-test) and Brazilian tensile tests (BT-test). The UCS-test model was 10 m long and 5 m wide, and the diameter of the BT-test model was 5 m, as shown in Figure 5. The average size of the blocks in the calibration numerical model was also set to 0.3 m, which was same as that of the region of interest. The calibrated micro-properties are presented in Table 2. The rock mass properties obtained from the calibrated simulation tests with the target values are shown in Table 3. It can be seen that the errors between the numerical results, including elastic modulus, uniaxial compressive strength and tensile strength, and the target values do not exceed 4%, indicating that the calibrated micro-properties are reasonable.

$$\frac{E_m}{E_r} = 10^{0.186RQD-1.91} \tag{1}$$

where E_m and E_r are the elastic modulus of rock mass and intact rock, respectively.

$$\frac{\sigma_{cm}}{\sigma_c} = \left(\frac{E_m}{E_r}\right)^n,\ \sigma_{tm} = \frac{1}{10}\sigma_{cm} \tag{2}$$

where σ_{cm}, σ_c and σ_{tm} are the uniaxial compressive strength of rock mass, the uniaxial compressive strength of intact rock, and the tensile strength of rock mass, respectively. n=0.63 was used in this study.

$$K_m = \frac{E_m}{3(1-2\mu)},\ G_m = \frac{E_m}{2(1+\mu)} \tag{3}$$

where K_m and G_m are the bulk and shear moduli of rock mass. μ is Poisson's ratio.

TABLE 1 Properties of intact rocks and rock masses.

Rock Strata	Intact Rock E_r (GPa)	σ_c (MPa)	RQD	Rock Mass E_m (GPa)	σ_{cm} (MPa)	σ_{tm} (MPa)
sandstone	9.5	61.2	90	5.5	43.5	3.62
Siltstone	6.9	45.4	85	3.2	28.2	2.35
Sandy mudstone	3.8	26.4	82	1.5	15.1	1.26
Coal	3.1	25.3	79	1.12	13.4	1.12

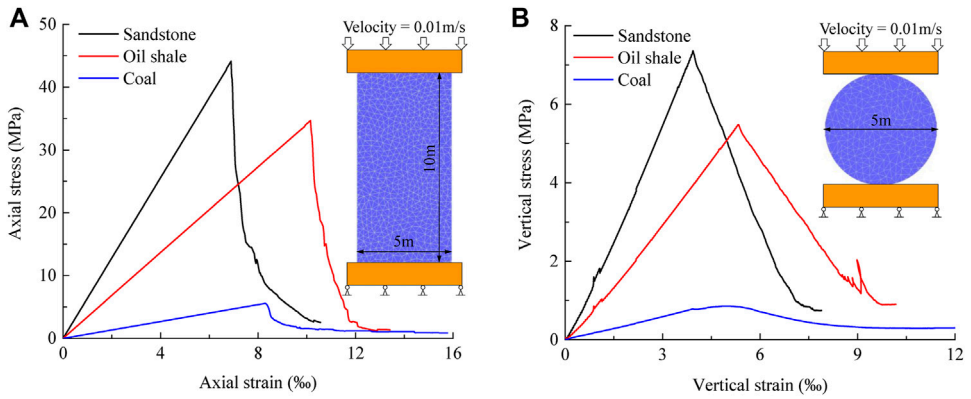

FIGURE 5
Calibration of mechanical parameters in the UDEC-Trigon model: **(A)** axial stress-strain curves for UCS-tests, and **(B)** vertical stress-strain curves for BT-tests.

TABLE 2 Calibrated micro-properties for UDEC-Trigon model.

Rock Strata	Matrix Properties E (GPa)	Contact Properties Poisson's Ratio	k_n (GPa/m)	k_s (GPa/m)	Cohesion (MPa)	Friction Angle (°)	Tensile Strength (MPa)
sandstone	9.5	0.26	225.0	67.5	14.1/0*	43/31*	3.30/0*
Siltstone	6.9	0.25	129.0	32.3	10.3/0*	39/32*	2.20/0*
Sandy mudstone	3.8	0.21	58.8	21.2	5.6/0*	37/31*	1.16/0*
Coal	3.1	0.21	84.3	30.4	5.1/0*	36/31*	0.98/0*

Peak and residual value.

$$k_n = n\left[\frac{K_m + (4/3)G_m}{\Delta Z_{\min}}\right](1 \le n \le 10),\ k_s = (0.25 - 0.4)k_n \quad (4)$$

where k_n and k_s are the normal stiffness and shear stiffness, respectively, $\Delta Z_{\min}$ is the smallest width of zone.

3.4 Model validation

The numerical model was validated by comparing the simulation results with the field measurements. Three important aspects are included in the validation: (1) deformation caused by the headentry excavation, (2) displacement of the top, bottom, RSR, and WFR of the headentry due to the MSTCB, and (3) failure characteristics of the headentry induced by the MSTCB. The simulated deformation caused by the excavation of the headentry was compared with the results measured during the field development, as shown in Figure 6A. It can be seen that they have the same trend, the rate of deformation decreased gradually, and the convergence between the top and bottom is greater than that between RSR and WFR. Deformation characteristics of the headentry after excavation are different from those in horizontal coal seams (Li et al., 2022). This is due to the fact that the top and bottom of the

TABLE 3 Target values and final simulation results for rock mass for UDEC-Trigon model.

Rock strata	E_m (GPa)			σ_{cm} (MPa)			σ_{tm} (MPa)		
	Target	Calibrated	Error (%)	Target	Calibrated	Error (%)	Target	Calibrated	Error (%)
sandstone	5.5	5.2	5	43.5	44.2	2	3.62	3.73	3
Siltstone	3.2	3.1	3	28.2	27.9	1	2.35	2.31	2
Sandy mudstone	1.5	1.5	0	15.1	15.7	4	1.26	1.28	2
Coal	1.12	1.05	6	13.4	13.7	2	1.12	1.15	3

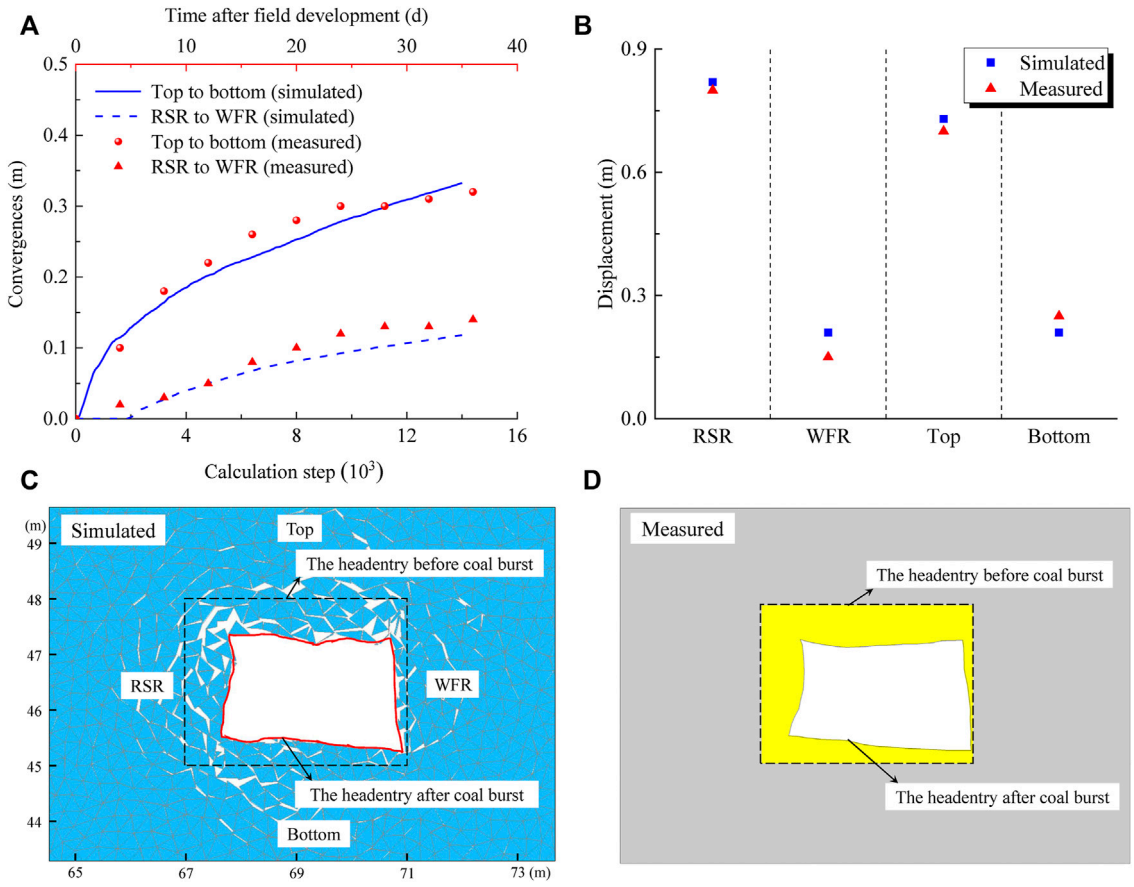

FIGURE 6
Validation of the UDEC-Trigon model: **(A)** convergence of the headentry, **(B)** displacement in the MSTCB, **(C)** simulated results of the MSTCB, and **(D)** measured results of the MSTCB.

headentry in this study are coal, rather than rock. The thickness of the top coal is greater than the width of the coal pillar in the RSR. Large deformation will occur in the top and bottom coal with increasing stress. As shown in Figure 6B, the simulated and measured results for the displacements of the top, bottom, RSR, and WFR of the headentry induced by the MSTCB are also very close, with the largest displacement of coal in the RSR. The failure characteristics of the simulated and *in-situ* coal burst are shown in Figures 6C, D, respectively. The same failure characteristics are shown with severe dynamic damage mainly at the top and RSR, and only minor damage in the WFR. The simulation results are in good agreement with the field measurements, indicating that the numerical model and simulation procedures adopted in this study can well reproduce the MSTCB process.

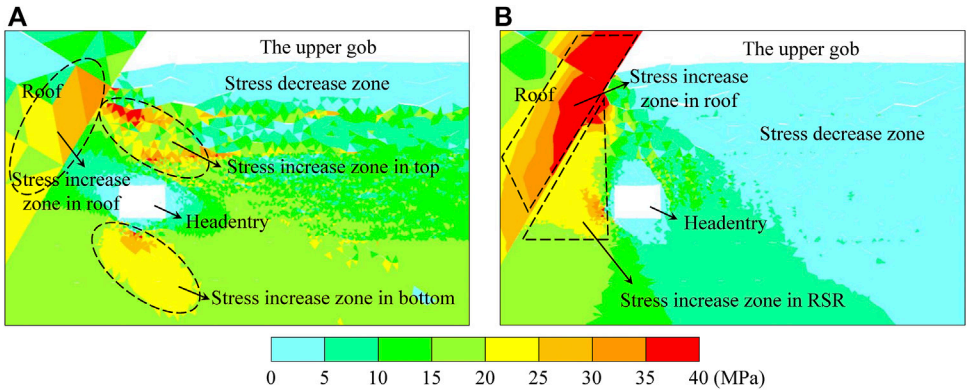

FIGURE 7
The stresses after the excavation of the upper mining section and the headentry: **(A)** horizontal stresses, and **(B)** vertical stresses.

4 Results and analysis

4.1 Stress evolution

The horizontal stresses and vertical stresses after the excavation of the upper mining section and the headentry are shown in Figure 7A and 7 B. The mining of the upper section resulted in a large stress decrease zone in the coal seam. However, the stress increase zone appeared in the roof due to the gradual falling and deforming of the roof caused by mining, and there were three stress increase zones in the coal around the headentry under the compression of the roof, they were the horizontal stress increase zone at the top, the horizontal stress increase zone at the bottom and the vertical stress increase zone located in the RSR. A large amount of elastic energy would accumulate in the stress concentration zone in the roof and coal, resulting in a potentially high risk of coal bursts. The above high coal burst risk zones have been validated by the MSTCB that occurred on June 29.

The propagation of the mining induced seismicity will cause stress changes in the rock or coal. As expected, the stresses in the coal around the headentry were changed under the action of the mining induced seismicity. Figure 8 presents the stress records of all the monitoring points after the dynamic calculation mode is activated, including the seismic wave propagation stage before the dynamic time of 0.06 s and the MSTCB stage after the dynamic time of 0.06 s. During the propagation stage, most of the monitoring points were recorded the stress increase caused by the seismic wave. These increased stresses are called dynamic stresses. As shown in Figures 9A,C, large dynamic stresses were recorded at each monitoring point at the top of the headentry and in the RSR, indicating that the mining induced seismicity in the roof had a significant effect on these two regions. The largest dynamic stresses were observed in the RSR, and accordingly, the most severe coal burst damage occurred in the RSR. The dynamic stresses at the bottom and shallow WFR (e.g., W1, W2 and W3) were small, indicating that the mining induced seismicity in the roof had a minor effect on these areas. However, the stresses at the monitoring points located in the deep part of the WFR (e.g., W4, W5 and W6) were not increased, indicating that the action range of the mining induced seismicity in the roof was limited in the WFR. As we know, the stresses will decrease significantly after a failure occurs. The stress drop is associated with the sudden penetration of cracks (Xue et al., 2020). During the MSTCB, the stresses at most of the monitoring points decreased, except for T3, B3, W4, W5, and W6. The stresses at W4, W5, and W6 increased because the coal burst occurred only in a limited shallow area in the WFR, causing the stresses to be transferred to the deeper part. The stresses in T3 and B3 did not decrease, probably due to some individual stress concentrations that occurred in localized areas during the MSTCB.

4.2 Cracking development

Many studies have shown that the microstructure of coal is influenced by many factors, resulting in a complex process of crack development (Xue et al., 2022; Zou et al., 2022; Xue et al., 2023). Figure 9A illustrates the distribution of cracks after mining of the upper section, with blue colour indicated tensile cracks and red colour shear cracks. The coal can be divided into two zones according to the majority of crack types: (1) shallow zone and (2) deep zone. In the shallow zone, most of the cracks were of the tensile failure type, which was due to the deformation of the coal in the shallow zone towards the upper mining area. However, in the deep zone, the coal was not only clamped by the roof and floor, but also constrained by the coal in the shallow zone. Therefore more shear slip occurred in the deep coal, resulting in most of the cracks being of shear failure type. In addition, it should be noted that the cracks did not extend to the area where the headentry is located, forming a

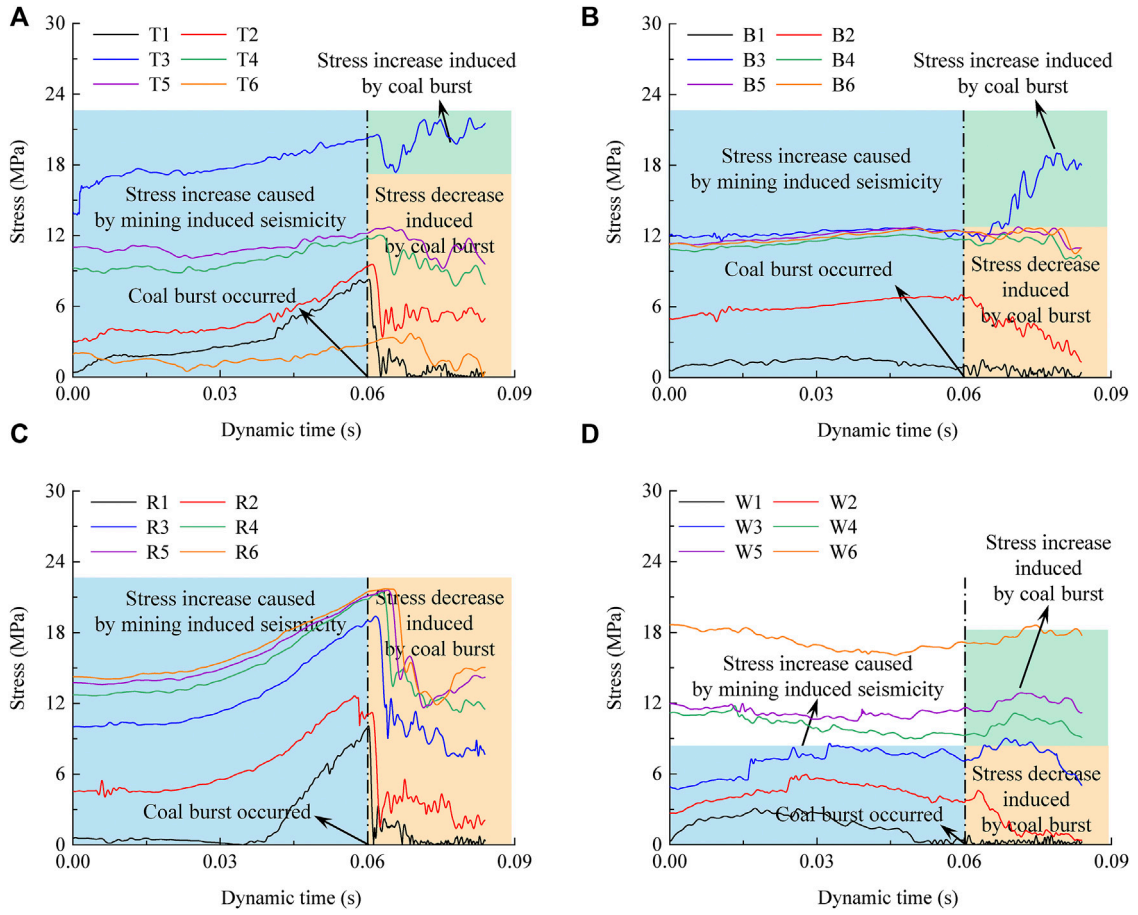

FIGURE 8
Stress changes around the 5,521–20 headentry during the MSTCB: **(A)** at the top, **(B)** at the bottom, **(C)** at RSR, and **(D)** at WFR.

triangular area where cracks are not developed. This is because the coal in the triangular area is subjected to compressive stresses under the clamping of the roof and floor, which has a higher strength.

Figures 9B–E present the crack development in the coal around the headentry during the MSTCB. As shown in Figure 9B, at the beginning of the MSTCB, a large number of shear cracks appeared first in the coal under the superposition of the initial high static stress and dynamic stress. When the dynamic time is 0.072 s, the shear cracks developed from the area near the headentry surface to the deeper part, as shown in Figure 9C. The dominant direction of crack development was west-east, which was the area of the top and RSR crossover, and this is because the static stress and dynamic stress in this area are both higher. In addition, the number of tensile cracks near the headentry surface gradually increased. Coal plate bending started to appear. As time increased, tensile cracks developed from the area near the headentry surface to the deeper part, as shown in Figure 9D. Eventually, the tensile failure zone near the headentry surface and the shear failure zone located at the deeper part were formed.

4.3 Ejection velocity patterns

Figure 10 illustrates the velocity vectors around the headentry at different dynamic times during the MSTCB, including the amplitude and direction of the ejection velocities. When the dynamic time was 0.066 s, the main high-velocity areas were the top and the RSR of the headentry, and the direction of the velocity vector radiated from the top to the headentry, indicating that the initial coal burst occurred at the top and the RSR under the action of the seismic wave from the roof. When the dynamic time was 0.072 s, the velocity of the headentry bottom located near the roof started to increase. As time increased, the range of the bottom coal burst and the amplitude of the ejection velocity gradually increased, indicating that the bottom coal burst occurred. There was no significant change in the velocity of the WFR during the MSTCB. Despite the small

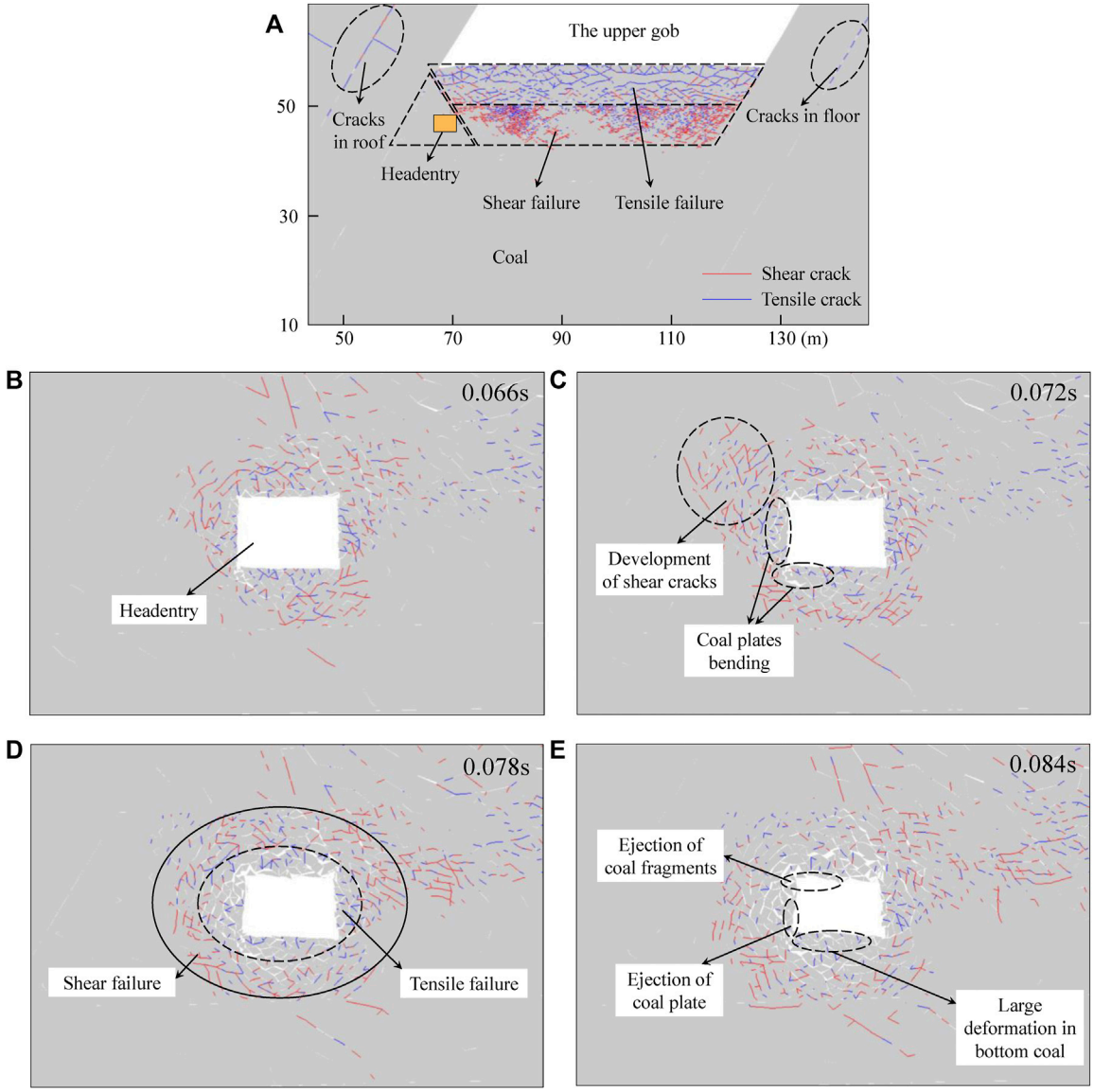

FIGURE 9
Crack development: **(A)** the cracks after mining of the upper section, **(B)** dynamic time is 0.066s in the MSTCB, **(C)** dynamic time is 0.072s in the MSTCB, **(D)** dynamic time is 0.078s in the MSTCB, and **(E)** dynamic time is 0.084s in the MSTCB.

time interval, the bottom coal burst occurred later than the top and RSR coal bursts in the MSTCB.

Figures 11A,B show the horizontal velocity and vertical velocity of the MSTCB obtained from the simulation. The high horizontal velocity region was the RSR and was larger compared to the WFR. The high vertical velocity regions were the top and the bottom near the roof. The regions of high ejection velocity due to the MSTCB were mainly the RSR, the top, and the bottom near the roof, which is consistent with the regions where severe dynamic failures were observed to occur in the field.

5 Discussion

5.1 Effect of the mining induced seismicity

Many studies have shown that high-energy mining induced seismicity plays an important role in coal bursts (He et al., 2012b; Wang et al., 2019a; Si et al., 2020). The vibration velocity of mining induced seismicity increases with the increase of its energy (He et al., 2015). In this study, numerical simulation results and analysis confirm that the dynamic stress caused by the mining induced

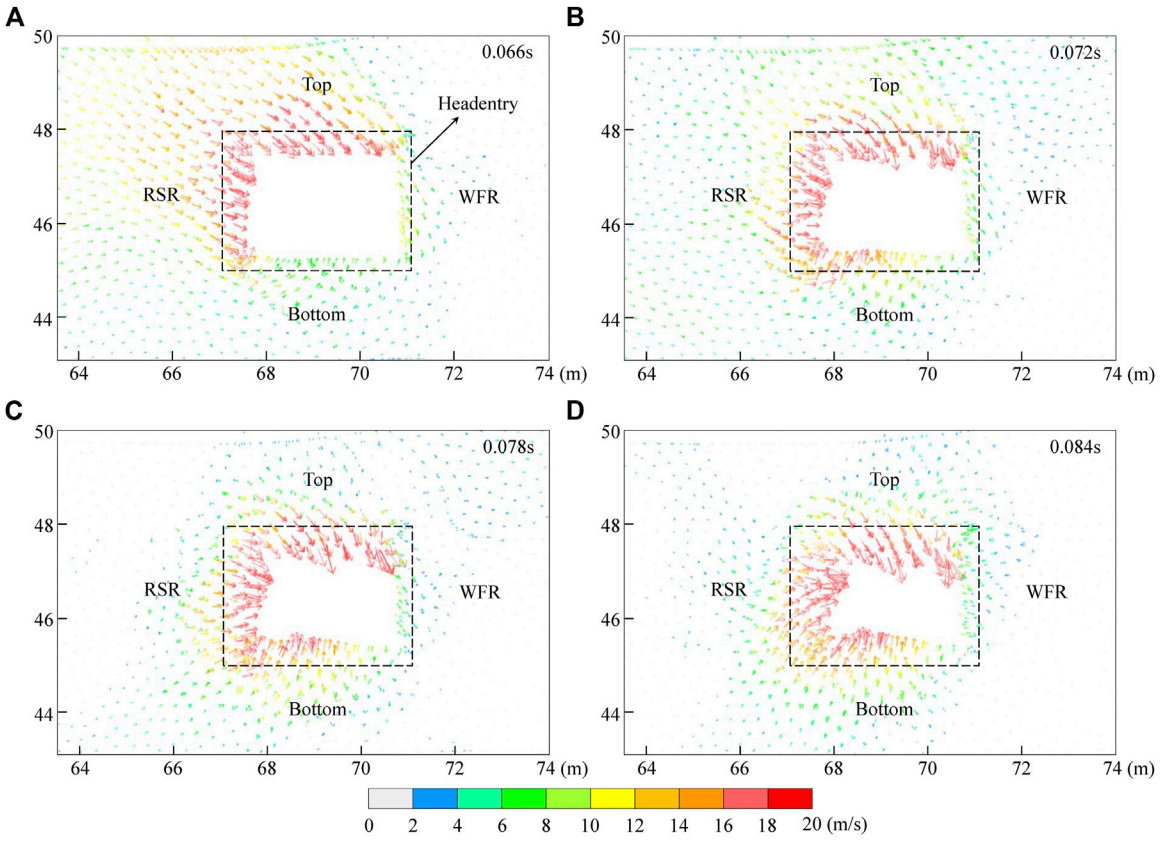

FIGURE 10
Velocity vectors around the headentry at different dynamic times: **(A)** dynamic time is 0.066s in the MSTCB, **(B)** dynamic time is 0.072s in the MSTCB, **(C)** dynamic time is 0.078s in the MSTCB, and **(D)** dynamic time is 0.084s in the MSTCB.

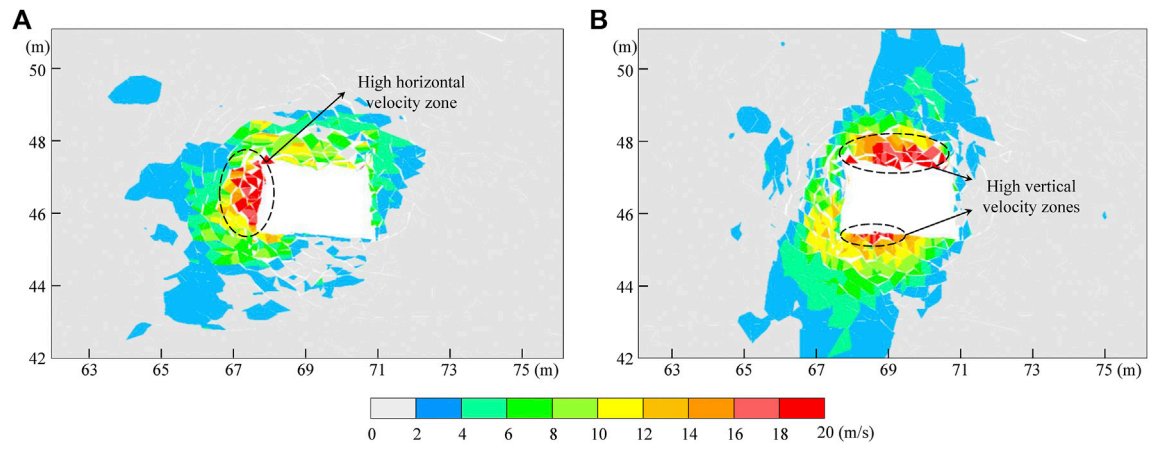

FIGURE 11
Ejection velocities of fragments in the MSTCB: **(A)** the horizontal ejection velocity, and **(B)** the vertical ejection velocity.

seismicity has an important effect on the MSTCB. It can be predicted that the dynamic stress will increase with the increase of the mining induced seismicity vibration velocity. However, the MSTCB in different areas of the headentry had significantly different failure characteristics. For example, quite severe coal bursts occurred at the top and in the RSR, while only a small amount of low-velocity

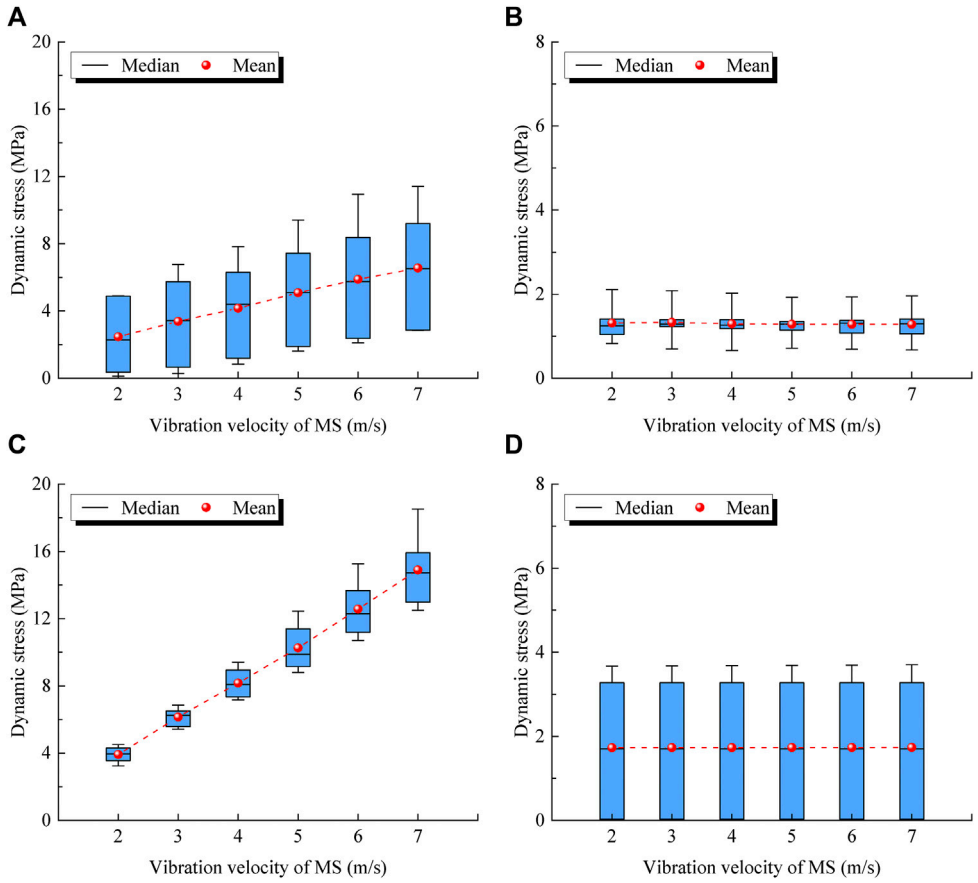

FIGURE 12
Dynamic stresses around the headentry considering different vibration velocities: **(A)** at the top, **(B)** at the bottom, **(C)** at RSR, and **(D)** at WFR.

ejections occurred in the WFR. Therefore the effect of the mining induced seismicity on coal bursts in different areas of the headentry needs to be further discussed. This can provide guidance for the determination of the critical areas for the MSTCB control in the headentry.

Figure 12 illustrates the relationship between dynamic stresses in different areas of the headentry and the vibration velocity of the mining induced seismicity, for any area, all six monitoring points are included. As shown in Figures 12A,C, the dynamic stresses in the top and RSR increased with the vibration velocity, indicating that the mining induced seismicity in the roof has a significant effect on the dynamic stresses in the top and RSR of the headentry. In addition, the growth rate of dynamic stress in the RSR is greater than that in the top. Therefore, the risk of the MSTCB in the RSR will increase significantly with the increase of vibration velocity. It is worth to be noted that the dynamic stresses in the bottom and WFR did not increase with increasing vibration velocity, and there was no significant change in the dynamic stresses in the bottom and WFR under different vibration velocities, as shown in Figures 12B,D. This is probably because the dynamic stresses in the bottom and WFR are mainly caused by the coal bursts in the top and RSR, rather than propagation of the seismic wave.

Figure 13 illustrates the relationship between ejection velocity and the vibration velocity in different areas of the headentry, for any area, all six monitoring points are included. As shown in Figures 13A and 13C, the injection velocity in the top and RSR increased with increasing vibration velocity, which is consistent with the results obtained in the laboratory (Li et al., 2021a). The result indicates that the mining induced seismicity in the roof is a key factor affecting the occurrence of coal bursts in the top and RSR of the headentry. However, the ejection velocity in the bottom and WFR did not increase significantly with increasing vibration velocity, as shown in Figures 13B and 13D. The reasons for the failures in the bottom and the WFR may be the transfer of stress and energy due to the development of the coal bursts at the top and the RSR. The maximum ejection velocity always occurs in the RSR, indicating that the RSR is the most dangerous area in the MSTCB.

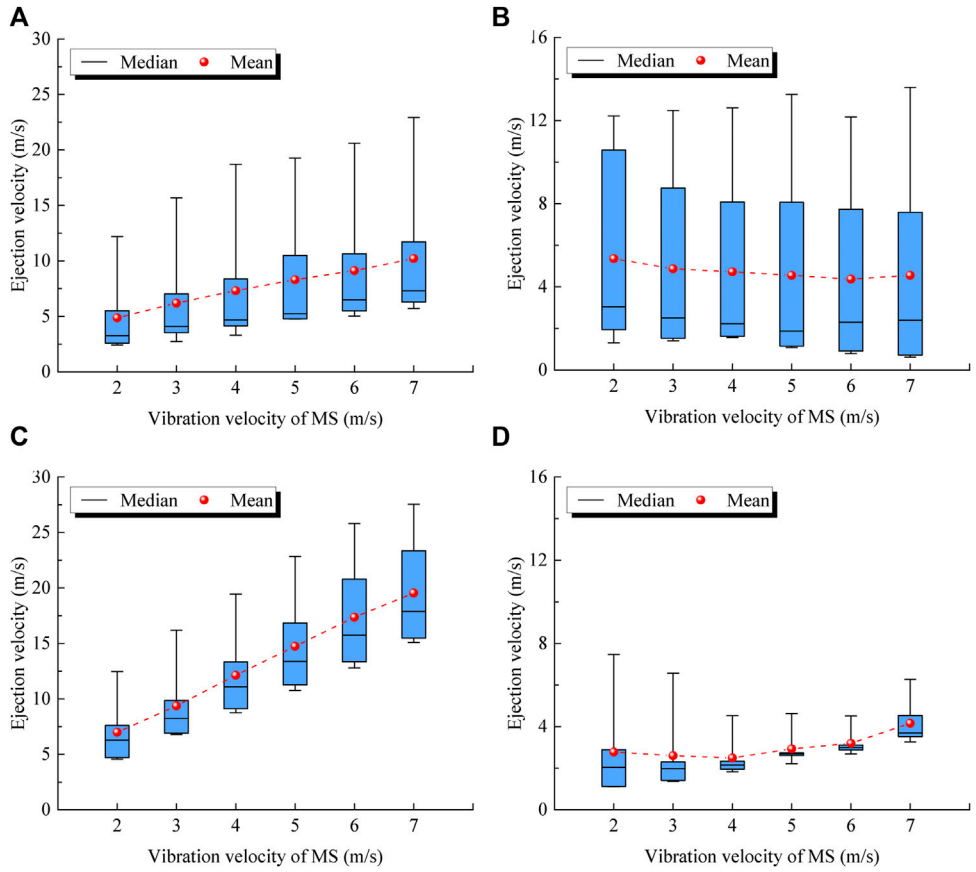

FIGURE 13
Ejection velocities around the headentry considering different vibration velocities: **(A)** at the top, **(B)** at the bottom, **(C)** at RSR, and **(D)** at WFR.

Many studies have reported the ejection velocity of coal fragments in coal bursts based on experimental observations or theoretical analysis. For example, (Yang et al., 2020a) proposed an ejection velocity estimation method and applied it to analyze a coal burst in an Australian coal mine, and found that the ejection velocity of fragments in the coal burst ranged from 26.55 to 26.62 m/s. Frith et al. (2020) analyzed a development coal burst and concluded that $3.8*10^4$ kg of coal was ejected at a velocity of 22 m/s during the coal burst. (Li et al., 2021a). measured the ejection velocity of fragments during coal bursts in the laboratory, and the results showed that most of the ejection velocities were in the range of 10–30 m/s. In this study, the maximum ejection velocities of coal fragments in MSTCBs under different vibration velocities were 12.47, 16.18, 19.45, 22.84, 25.82, and 27.53 m/s. The simulation ejection velocities are in good agreement with the mentioned findings.

5.2 Failure mechanism

As shown in Figure 14, a large destress zone is formed except for a triangular zone on the roof side. The coal burst risk in the destress zone is significantly reduced. There is a high initial static stress σ_{s-i} in the triangular zone under the clamping of the roof and floor, causing a high risk of coal bursts. A steeply inclined cantilever beam is formed in the roof and the length of the cantilever beam gradually increases with the section mining, resulting in a tendency for the cantilever beam to rotate toward the gob. However, the rotation is restricted by the coal in the triangular zone. Therefore, additional static stress will be formed in the triangular zone, which is called mining-induced static stress σ_{s-m}. The superposition of the initial static stress and the mining-induced static stress leads to the formation of high static stresses in the coal on the roof side. In addition, high-energy mining induced seismicity often occurs during the mining of SIETCS. The propagation of high-energy mining induced seismicity causes dynamic stress σ_d. The MSTCBs occur when the superposition of the initial static stress, the mining-induced static stress and the dynamic stress exceeds the ultimate strength of the coal σ_u, as shown in Eq. 5.

$$\sigma_{s-i} + \sigma_{s-m} + \sigma_d \geq \sigma_u \tag{5}$$

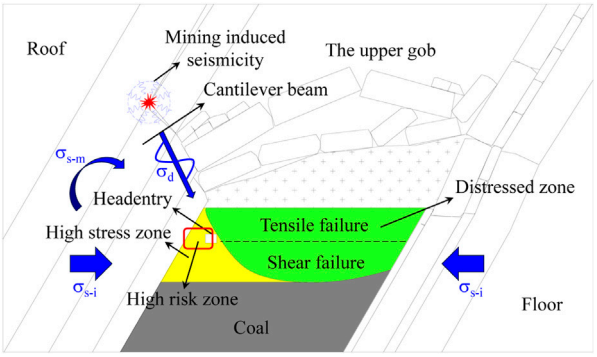

FIGURE 14
The mechanism of the MSTCB in SIETCS.

where σ_{s-i}, σ_{s-m}, and σ_d are the initial static stress, the mining-induced static stress and the dynamic stress. And σ_u is the ultimate strength of the coal.

5.3 Coal burst control in the headentry

The high risk areas for MSTCBs in the headentry were identified as the top, RSR, and the bottom near the roof. Accordingly, the MSTCB prevention measures were proposed, as shown in Figure 15A. High-energy mining induced seismicity in the roof plays a critical role for MSTCBs. Therefore, pre-splitting blasting was applied to the roof to avoid the occurrence of high-energy mining induced seismicity caused by a large-scale breakage of the roof. In addition, a number of measures including large diameter drilling and blasting in the coal were employed to create destress zones. It should be noted that the spacing of the boreholes in the RSR is smaller compared to the WFR. The design parameters are shown in Table 4.

Mining induced seismicity monitoring was performed at the 5,521-20 working face through a micro-seismic monitoring system. As shown in Figure 15B, the change in total energy presents a periodical characteristic, which is related to the periodic adjustment of the structure in the roof. The total energy increases significantly when the structure experiences change. After the application of pre-splitting, the number of seismic events with energy greater than 10^4 J decreased significantly and the number of low-energy seismic events increased. This is because pre-cracks formed in the roof after pre-splitting blasting, which will develop under abutment pressure. The sudden large scale fracturing is replaced by the development of pre-cracks. The stress in the coal will increase under the effect of high-energy seismic events. In addition, the failure of the structure is more likely to be triggered by high-energy seismic events. Thus, the decrease in high-energy seismic events indicates a reduction in coal burst risk. Mining practice at the 5521-20 working face demonstrates that the measures are effective for the prevention and control of MSTCBs in SIETCSs.

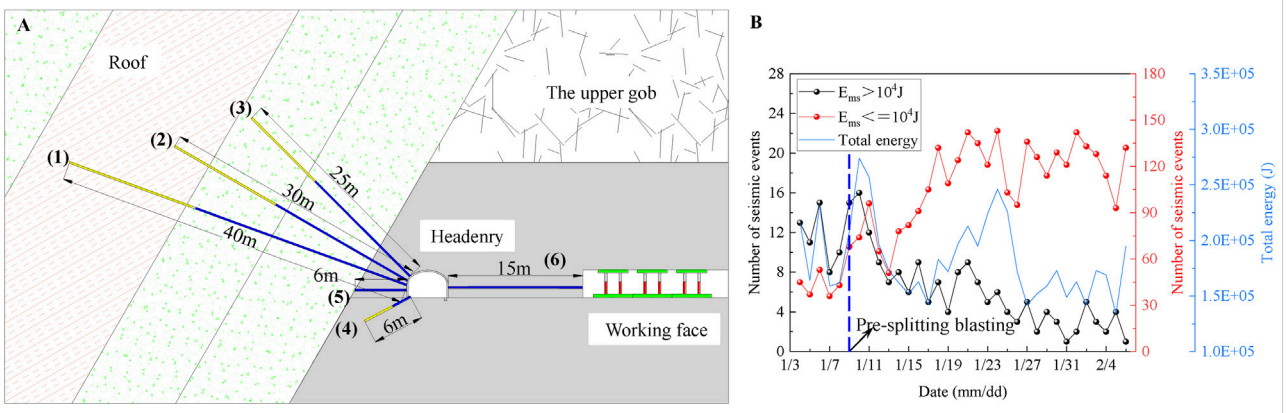

FIGURE 15
Prevention measures for MISTCB and monitoring results of the mining induced seismic events: **(A)** prevention measures for MISTCB, **(B)** monitoring results of the mining induced seismic events.

TABLE 4 Design parameters for boreholes 1#—6# (see Figure 15A).

Number	Angle (°)	Distance between Boreholes (m)	Diameter of Borehole (mm)	Length of Borehole (m)	Explosive Charge Length (m)	Sealing Length (m)
1	20	20	75	40	15	25
2	30	20	75	30	13	17
3	45	20	75	25	10	15
4	30	5	75	6	3.5	2.5
5	0	5	110	6	/	/
6	0	10	110	15	/	/

6 Conclusion

In this paper, the dynamic failure process of the MSTCB in SIETCS is investigated using UDEC simulation based on a coal burst accident. And the effect of mining induced seismicity vibration velocity on MSTCBs in SIETCSs is discussed. The main conclusions are as follows.

1) A large destress zone is formed in the SIETCS after section mining, except for a triangular area on the roof side. The triangular area is undeveloped with cracks and has a good capacity for storing stress and energy, which causes a high coal burst risk. During the MSTCB, a large number of shear cracks appear first near the roadway surface. Then, the cracks develop rapidly to the depth. Eventually, the MSTCB leads to the formation of a tensile failure zone near the roadway surface and a shear failure zone at the deeper part, respectively.
2) The mechanism of the MSTCB is: under the effect of the cantilever beam rotation, as a pivot point, the coal on the roof side in SIETCS is in high static stress. And high-energy mining induced seismicity in the roof causes additional dynamic stress on the coal, especially at the RSR and top of the roadway. MSTCB occurs as the superposition of the static stress and the dynamic stress exceeds the ultimate strength of the coal.
3) The vibration velocity of mining induced seismicity in the roof has a significant and asymmetric effect on the MSTCB in SIETCS. The dynamic stress and mean ejection velocity in the RSR and top of the roadway are positively correlated with the vibration velocity. However, the vibration velocity only has a weak effect on the WFR and bottom of the roadway.

Data availability statement

The original contributions presented in the study are included in the article/supplementary material, further inquiries can be directed to the corresponding authors.

Author contributions

All authors listed have made a substantial, direct, and intellectual contribution to the work and approved it for publication. Conceptualization: JC, LD, and JH; Methodology: JC and GZ; Software: LD; Validation: JC and JH; Formal Analysis: JC, JH, and ZW; Investigation: JC, GZ, and JB; Data curation: JC, ZH, and ZW; Writing-Original Draft Preparation: JC; Writing-Review & Editing: ZH and JB; Supervision: JC, LD, and GZ; Project Administration: LD and GZ; Funding Acquisition: LD and GZ. All authors have read and agreed to the published version of the manuscript.

Funding

This work was conducted with support from the National Natural Science Foundation of China (Grant Nos. 51934007, 51874292, and 51904235).

Acknowledgments

The first author JC would like to express his sincere thanks to the China Scholarship Council (CSC) for the financial support for his study at TU Bergakademie Freiberg, Germany.

Conflict of interest

The authors declare that the research was conducted in the absence of any commercial or financial relationships that could be construed as a potential conflict of interest.

Publisher's note

All claims expressed in this article are solely those of the authors and do not necessarily represent those of their affiliated organizations, or those of the publisher, the editors and the reviewers. Any product that may be evaluated in this article, or claim that may be made by its manufacturer, is not guaranteed or endorsed by the publisher.

References

Cai, W., Dou, L., Si, G., and Hu, Y. (2021). Fault-induced coal burst mechanism under mining-induced static and dynamic stresses. *Engineering* 7 (5), 687–700. doi:10.1016/j.eng.2020.03.017

Cao, J., Dou, L., Zhu, G., He, J., Wang, S., and Zhou, K. (2020). Mechanisms of rock burst in horizontal section mining of a steeply inclined extra-thick coal seam and prevention technology. *Energies* 13 (22), 6043. doi:10.3390/en13226043

Cui, F., Lei, Z., Chen, J., Bo, C., Yang, Y., Changlu, L., et al. (2019). Research on reducing mining-induced disasters by filling in steeply inclined thick coal seams. *Sustainability* 11 (20), 5802. doi:10.3390/su11205802

Dai, L., Pan, Y., Li, Z., Wang, A., Xiao, Y., Liu, F., et al. (2021). Quantitative mechanism of roadway rockbursts in deep extra-thick coal seams: Theory and case histories. *Tunn. Undergr. Space Technol.* 111, 103861. doi:10.1016/j.tust.2021.103861

Dou, L., and He, X. (2001). *Theory and technology of rock burst prevention*. Xuzhou: China University of Mining and Technology Press.

Dou, L., Mu, Z., Li, Z., Cao, A., and Gong, S. (2014). Research progress of monitoring, forecasting, and prevention of rockburst in underground coal mining in China. *Int. J. Coal Sci. Technol.* 1 (3), 278–288. doi:10.1007/s40789-014-0044-z

Dou, L., He, J., Cao, A., Gong, S., and Cai, W. (2015). Rock burst prevention methods based on theory of dynamic and static combined load induced in coal mine. *J. China Coal Soc.* 40 (7), 1469–1476. doi:10.13225/j.cnki.jccs.2014.1815

Du, F., Wang, K., Zhang, X., Xin, C., Shu, L., and Wang, G. (2020). Experimental study of coal–gas outburst: Insights from coal–rock structure, gas pressure and adsorptivity. *Nat. Resour. Res.* 29 (4), 2481–2493. doi:10.1007/s11053-020-09621-7

Frith, R., Reed, G., and Jones, A. (2020). A causation mechanism for coal bursts during roadway development based on the major horizontal stress in coal: Very specific structural geology causing a localised loss of effective coal confinement and Newton's second law. *Int. J. Min. Sci. Technol.* 30 (1), 39–47. doi:10.1016/j.ijmst.2019.12.018

Gao, F. Q., and Stead, D. (2014). The application of a modified Voronoi logic to brittle fracture modelling at the laboratory and field scale. *Int. J. Rock Mech. Min. Sci.* 68, 1–14. doi:10.1016/j.ijrmms.2014.02.003

Gao, F., and Yang, L. (2021). Experimental and numerical investigation on the role of energy transition in strainbursts. *Rock Mech. Rock Eng.* 54 (9), 5057–5070. doi:10.1007/s00603-021-02550-8

Gao, F., Stead, D., and Kang, H. (2014). Numerical simulation of squeezing failure in a coal mine roadway due to mining-induced stresses. *Rock Mech. Rock Eng.* 48 (4), 1635–1645. doi:10.1007/s00603-014-0653-2

He, J., Dou, L.-M., Cai, W., Li, Z.-L., and Ding, Y.-L. (2015). *In situ* test study of characteristics of coal mining dynamic load. *Shock Vib.* 2015, 1–8. doi:10.1155/2015/121053

He, J., Dou, L., Gong, S., Li, J., and Ma, Z. (2017). Rock burst assessment and prediction by dynamic and static stress analysis based on micro-seismic monitoring. *Int. J. Rock Mech. Min. Sci.* 93, 46–53. doi:10.1016/j.ijrmms.2017.01.005

He, S., Song, D., Li, Z., He, X., Chen, J., Li, D., et al. (2019). Precursor of spatio-temporal evolution law of MS and AE activities for rock burst warning in steeply inclined and extremely thick coal seams under caving mining conditions. *Rock Mech. Rock Eng.* 52 (7), 2415–2435. doi:10.1007/s00603-018-1690-z

He, S., Song, D., He, X., Chen, J., Ren, T., Li, Z., et al. (2020). Coupled mechanism of compression and prying-induced rock burst in steeply inclined coal seams and principles for its prevention. *Tunn. Undergr. Space Technol.* 98, 103327. doi:10.1016/j.tust.2020.103327

He, H., Dou, L., Fan, J., Du, T., and Sun, X. (2012a). Deep-hole directional fracturing of thick hard roof for rockburst prevention. *Tunn. Undergr. Space Technol.* 32, 34–43. doi:10.1016/j.tust.2012.05.002

He, J., Dou, L., Cao, A., Gong, S., and Lü, J. (2012b). Rock burst induced by roof breakage and its prevention. *J. Cent. South Univ.* 19 (4), 1086–1091. doi:10.1007/s11771-012-1113-3

Jiang, Y., Zhao, Y., Wang, H., and Zhu, J. (2017). A review of mechanism and prevention technologies of coal bumps in China. *J. Rock Mech. Geotechnical Eng.* 9 (1), 180–194. doi:10.1016/j.jrmge.2016.05.008

Konicek, P., Saharan, M. R., and Mitri, H. (2011). Destress blasting in coal mining – state-of-the-art review. *Procedia Eng.* 26, 179–194. doi:10.1016/j.proeng.2011.11.2157

Konicek, P., Soucek, K., Stas, L., and Singh, R. (2013). Long-hole destress blasting for rockburst control during deep underground coal mining. *Int. J. Rock Mech. Min. Sci.* 61, 141–153. doi:10.1016/j.ijrmms.2013.02.001

Lai, X., Yang, Y., and Zhang, L. (2021). Research on structural evolution and microseismic response characteristics of overlying strata during repeated mining of steeply inclined and extra thick coal seams. *Lithosphere* 2021 (4), 8047321. doi:10.2113/2021/8047321

Li, Y., Yang, R., Fang, S., Lin, H., Lu, S., Zhu, Y., et al. (2022). Failure analysis and control measures of deep roadway with composite roof: A case study. *Int. J. Coal Sci. Technol.* 9 (1), 2. doi:10.1007/s40789-022-00469-1

Li, J., Zhao, J., Gong, S. Y., Wang, H. C., Ju, M. H., Du, K., et al. (2021a). Mechanical anisotropy of coal under coupled biaxial static and dynamic loads. *Int. J. Rock Mech. Min. Sci.* 143, 104807. doi:10.1016/j.ijrmms.2021.104807

Li, Z., He, S., Song, D., He, X., Dou, L., Chen, J., et al. (2021b). Microseismic temporal-spatial precursory characteristics and early warning method of rockburst in steeply inclined and extremely thick coal seam. *Energies* 14 (4), 1186. doi:10.3390/en14041186

Mark, C. (2018). Coal bursts that occur during development: A rock mechanics enigma. *Int. J. Min. Sci. Technol.* 28 (1), 35–42. doi:10.1016/j.ijmst.2017.11.014

Mottahedi, A., and Ataei, M. (2019). Fuzzy fault tree analysis for coal burst occurrence probability in underground coal mining. *Tunn. Undergr. Space Technol.* 83, 165–174. doi:10.1016/j.tust.2018.09.029

Ptáček, J. (2017). Rockburst in ostrava-karvina coalfield. *Procedia Eng.* 191, 1144–1151. doi:10.1016/j.proeng.2017.05.289

Qian, M., Miao, X., and Xu, J. (2000). *Key strata theory in ground control*. Xuzhou: China University of Mining and Technology Press.

Shapiro, S. A., Dinske, C., and Rothert, E. (2006). Hydraulic-fracturing controlled dynamics of microseismic clouds. *Geophys. Res. Lett.* 33 (14), L14312. doi:10.1029/2006gl026365

Si, G., Cai, W., Wang, S., and Li, X. (2020). Prediction of relatively high-energy seismic events using spatial–temporal parametrisation of mining-induced seismicity. *Rock Mech. Rock Eng.* 53 (11), 5111–5132. doi:10.1007/s00603-020-02210-3

Singh, M., and Seshagiri Rao, K. (2005). Empirical methods to estimate the strength of jointed rock masses. *Eng. Geol.* 77 (1-2), 127–137. doi:10.1016/j.enggeo.2004.09.001

Stec, K. (2007). Characteristics of seismic activity of the upper silesian coal basin in Poland. *Geophys. J. Int.* 168 (2), 757–768. doi:10.1111/j.1365-246x.2006.03227.x

Wang, K., and Du, F. (2020). Coal-gas compound dynamic disasters in China: A review. *Process Saf. Environ. Prot.* 133, 1–17. doi:10.1016/j.psep.2019.10.006

Wang, C., Cao, A., Zhang, C., and Canbulat, I. (2019a). A new method to assess coal burst risks using dynamic and static loading analysis. *Rock Mech. Rock Eng.* 53 (3), 1113–1128. doi:10.1007/s00603-019-01968-5

Wang, S., Dou, L., Mu, Z., Cao, J., and Li, X. (2019b). Study on roof breakage-induced roadway coal burst in an extrathick steeply inclined coal seam. *Shock Vib.* 2019, 1–14. doi:10.1155/2019/2969483

Wang, Z., Dou, L., and Wang, G. (2019c). Coal burst induced by horizontal section mining of a steeply inclined, extra-thick coal seam and its prevention: A case study from Yaojie No. 3 coal mine, China. *Shock Vib.* 2019, 1–13. doi:10.1155/2019/8469019

Wang, S.-C., Dou, L.-M., Wang, Z.-Y., Bai, J.-Z., and Chai, Y.-J. (2020). Mechanism of coal bursts induced by horizontal section mining of steeply inclined coal seams and application of microseismic multiparameter monitoring in early warning. *Adv. Civ. Eng.* 2020, 1–14. doi:10.1155/2020/1048624

Wang, S., Cao, A., Wang, Z., Cao, J., Liu, Y., Xue, C., et al. (2022). Study on mechanism of rock burst in horizontal section mining of a steeply inclined extra-thick coal seam. *Lithosphere* 2022 (11), 7058797. doi:10.2113/2022/7058797

Xie, P., Luo, Y., Wu, Y., Gao, X., Luo, S., and Zeng, Y. (2019). Roof deformation associated with mining of two panels in steeply dipping coal seam using subsurface subsidence prediction model and physical simulation experiment. *Min. Metallurgy Explor.* 37 (2), 581–591. doi:10.1007/s42461-019-00156-x

Xue, D., Zhou, J., Liu, Y., and Gao, L. (2020). On the excavation-induced stress drop in damaged coal considering a coupled yield and failure criterion. *Int. J. Coal Sci. Technol.* 7 (1), 58–67. doi:10.1007/s40789-020-00299-z

Xue, Y., Liu, J., Ranjith, P. G., Gao, F., Xie, H., and Wang, J. (2022). Changes in microstructure and mechanical properties of low-permeability coal induced by pulsating nitrogen fatigue fracturing tests. *Rock Mech. Rock Eng.* doi:10.1007/s00603-022-03031-2

Xue, Y., Ranjith, P. G., Chen, Y., Cai, C., Gao, F., and Liu, X. (2023). Nonlinear mechanical characteristics and damage constitutive model of coal under CO2 adsorption during geological sequestration. *Fuel* 331, 125690. doi:10.1016/j.fuel.2022.125690

Yang, S., Li, L., and Deng, X. (2019). Disaster-causing mechanism of roof "toppling–slumping" failure in a horizontal sublevel top-coal caving face. *Nat. Hazards (Dordr).* 100 (2), 757–780. doi:10.1007/s11069-019-03841-8

Yang, X., Ren, T., and Tan, L. (2020a). Estimation of average ejection velocity generated by rib burst under compression load. *Int. J. Rock Mech. Min. Sci.* 128, 104277. doi:10.1016/j.ijrmms.2020.104277

Yang, Y., Lai, X., Shan, P., and Cui, F. (2020b). Comprehensive analysis of dynamic instability characteristics of steeply inclined coal-rock mass. *Arab. J. Geosci.* 13 (6), 241. doi:10.1007/s12517-020-5217-z

Yun, D., Liu, Z., Cheng, W., Fan, Z., Wang, D., and Zhang, Y. (2017). Monitoring strata behavior due to multi-slicing top coal caving longwall mining in steeply dipping extra thick coal seam. *Int. J. Min. Sci. Technol.* 27 (1), 179–184. doi:10.1016/j.ijmst.2016.11.002

Zhang, L., and Einstein, H. H. (2004). Using RQD to estimate the deformation modulus of rock masses. *Int. J. Rock Mech. Min. Sci.* 41 (2), 337–341. doi:10.1016/s1365-1609(03)00100-x

Zhang, C., Canbulat, I., Hebblewhite, B., and Ward, C. R. (2017). Assessing coal burst phenomena in mining and insights into directions for future research. *Int. J. Coal Geol.* 179, 28–44. doi:10.1016/j.coal.2017.05.011

Zou, Q., Zhang, T., Ma, T., Tian, S., Jia, X., and Jiang, Z. (2022). Effect of water-based SiO2 nanofluid on surface wettability of raw coal. *Energy* 254, 124228. doi:10.1016/j.energy.2022.124228